Research Article

Nano Research
2023, 16(8): 11084–11095

ISSN 1998-0124 CN 11-5974/O4
https://doi.org/10.1007/s12274-023-5511-7

A finite oxidation strategy for customizing heterogeneous interfaces to enhance magnetic loss ability and microwave absorption of Fe-cored carbon microcapsules

Meixi Zhang[1,§], Laisen Wang[2,§], Susu Bao[1], Zhijia Song[1], Wenjiao Chen[1], Zhiyuan Jiang[1] (✉), Zhaoxiong Xie[1], and Lansun Zheng[1]

[1] *State Key Laboratory for Physical Chemistry of Solid Surfaces, College of Chemistry and Chemical Engineering, Xiamen University, Xiamen 361005, China*
[2] *College of Materials, Xiamen University, Xiamen 361005, China*
[§] *Meixi Zhang and Laisen Wang contributed equally to this work.*

Received: 9 December 2022 / **Revised:** 10 January 2023 / **Accepted:** 16 January 2023

ABSTRACT

Metallic iron particles are of great potential for microwave absorption materials due to their strong magnetic loss ability. However, the oxidation susceptibility of metallic iron particles in the atmospheric environment is regarded as a major factor causing performance degradation. Although many efforts have been developed to avoid their oxidation, whether partial surface oxidized iron particles can improve the microwave absorbing performance is rarely concerned. In order to explore the effect of partial surface oxidation of iron on its properties, the designed yolk–shelled (Fe/FeO_x)@C composites with multiple heterointerfaces were synthesized via an *in-situ* polymerization and a finite reduction–oxidation process of Fe_2O_3 ellipsoids. The performance enhancement mechanisms of Fe/FeO_x heterointerfaces were also elaborated. It is demonstrated that the introduction of Fe-based heterogeneous interfaces can not only enhance the dielectric loss, but also increase the imaginary part of the permeability in the higher frequency range to strengthen the magnetic loss ability. Meanwhile, the yolk–shell structure can effectively improve impedance matching and enhance microwave absorption performances via increasing multiple reflection and scattering behaviors of incident microwaves. Compared to Fe@C composite, the effective absorption (reflection loss (RL) < −10 dB) bandwidth of the optimized (Fe/FeO_x)@C-2 increases from 5.7 to 7.3 GHz (10.7–18.0 GHz) at a same matching thickness of 2 mm, which can completely cover Ku-band. This work offers a good perspective for the enhancement of magnetic loss ability and microwave absorption performance of Fe-based microwave absorption materials with promising practical applications.

KEYWORDS

heterogeneous interfaces, finite oxidation, yolk–shell structure, magnetic loss, interface polarization, microwave absorption

1 Introduction

Microwave absorbing materials (MAMs) have widespread applications in military stealth, communication security, electromagnetic protection, and other fields [1–8]. Among them, metallic iron particles are of great potential for microwave absorption (MA) due to their strong magnetic loss ability generated by large saturation magnetization (M_s) and high complex permeability in GHz range [9]. It is widely believed that the oxidation of metallic iron particles can result in decreased magnetic loss ability and narrowed effective absorption bandwidth (EAB) [10]. To protect the metallic iron particles from oxidation and make them keep stable performance in atmospheric environment, various Fe-cored nanostructures have been developed, with the shells made of SiO_2 [11, 12], semiconductor oxides [13], phosphates [14], carbon materials [15], and so on. However, in fact, the slight surface oxidation may promote the improvement of microwave absorption performance. Some interesting phenomena can be induced by the exchange coupling of ferromagnetic iron and antiferromagnetic/ferromagnetic iron oxides, which are rarely discussed, especially how they affect the permeability of the composite. When a ferromagnet (FM) is close to an antiferromagnet (AFM) or a ferrimagnet (FI) with a relatively larger magnetocrystalline anisotropy, the spins in the AFM or FI will play a pinning effect to hinder the rotation of the spins in the FM under a reversed magnetic field [16, 17]. Thus, an increase of coercivity (H_c) is realized which can make a significant effect on the permeability of the composite, and the influence mechanism is a worthwhile topic what we need to discuss. Moreover, the rich defects in iron/iron oxides heterointerfaces are proved to strengthen polarization loss (ε_p'') by inducing the aggregation or rearrangement of charge carriers and providing abundant active sites for polarization relaxation process [18, 19]. Meanwhile, the presence of interfaces facilitates the change of the electrons transmission mode and contributes to the conduction loss (ε_c'') [20]. For instance, Liu et al. fabricated carbonyl iron powder (CIP)/Fe_3O_4 composites with Fe_3O_4 shell and CIP core,

Address correspondence to zyjiang@xmu.edu.cn

and an optimal EAB of 6.3 GHz (8.7–15.0 GHz) was obtained [21]. Wang et al. prepared Fe/Fe_3O_4 composites via a simple one-pot solvothermal method, which showed an integrated absorption band (3.6–18 GHz) in a thickness (*d*) range of 1.4–5 mm [22]. Therefore, there is a possibility that the microwave absorption performance of the metallic iron particles can be improved by partial surface oxidation. Whereas, the drawbacks of high density and severe aggregation problem of Fe-based absorbers still hinder their practical applications [23].

Enfolding magnetic cores in carbon materials to form core–shell structures is a reliable solution to reduce the filling ratio of magnetic component and improve the dispersion of magnetic particles [24, 25]. Furthermore, it also offers a chance to optimize the impedance matching and strengthen dielectric loss ability to improve MA performance. Over the past decade, great efforts have been made to fabricate various core–shell structured composites with Fe-based magnetic cores and carbon shells, such as $FeNi_3$@C [26], Fe/void/C [27], CoFe/C [28], Fe/Fe_3C@graphite-C [29], and heterostructured Fe_3O_4/Fe@C [30]. For most of ferromagnetic/carbon composites, the relative complex permittivity is much higher than the relative complex permeability and that makes it difficult to realize perfect impedance matching. Although the permittivity of the composite can be easily tailored by controlling the content of carbon materials, it is hard to increase permeability or even maintain it as the frequency (*f*) increases due to the Snoek's limit and large eddy-current effects. Usually, the permeability can be improved by modifying the intrinsic parameters (such as saturation magnetization, magnetocry-stalline anisotropy constant, and internal strain) or adjusting the morphology and size of the MAMs (such as nano-materialization, flattening, and fibering). For example, Zhou et al. prepared flaky FeSiAl powders with enhanced complex permeability by increasing the shape anisotropy of samples through a ball milling process [31]. Liu et al. prepared $Nd(Fe_{1-x}Co_x)_{10}V_2$ compounds with different Co contents, and samples with x = 0.2 and x = 0.3 show higher complex permeability due to the improvement of saturation magnetization [32]. However, few attempts have been made to improve the MA performance of the composite in terms of improving the imaginary part of complex permeability by a deliberate surface oxidation treatment. It remains a great challenge to improve the permeability and elucidate their performance enhancement mechanisms for optimizing the MA performance of Fe-cored carbon composites.

In this work, a finite oxidation strategy has been developed to prepare a series of yolk–shelled (Fe/FeO_x)@C composites with rich heterogeneous interfaces using Fe_2O_3@polydopamine (PDA) as precursors. The controlled carbon composition and finite reduction–oxidation process lead to the transition of Fe_2O_3 to different magnetic cores (Fe/FeO, Fe/Fe_3O_4, and Fe). The influence mechanisms of Fe/FeO_x heterointerfaces on the permeability and performance enhancement of the composites are fully discussed. It is revealed that a slight oxidation is beneficial to improve the MA performance of the ferromagnetic iron by increasing the imaginary part of the permeability in the higher frequency range, which provides a new insight into the development of ferromagnetic/carbon materials with broad-band effective absorption at a small thickness.

2 Experimental

2.1 Materials

Iron trichloride hexahydrate ($FeCl_3·6H_2O$, ≥ 99.0%), sodium hydroxide (NaOH, ≥ 96.0%), ethanol absolute (C_2H_5OH, ≥ 97.0%), and dopamine hydrochloride ($C_8H_{11}NO_2$·HCl, ≥ 99.0%) were supplied by Chemical Reagent Co., Ltd. All chemicals were not purified before using.

2.2 Synthesis of Fe_2O_3 particles

Typically, a wine-red solution containing 16 mL C_2H_5OH, 32 mL water (H_2O), 10.80 g $FeCl_3·6H_2O$, and 0.68 g NaOH was added to a 100 mL Teflon-lined stainless steel autoclave. Then, the autoclave was put in an oven and maintained at 160 °C for 12 h. The obtained purple precipitate was harvested by centrifugation and washed by distilled water and C_2H_5OH alternately, then dried in an oven at 70 °C for 24 h.

2.3 Synthesis of Fe_2O_3@PDA composites

The Fe_2O_3@PDA precursors were obtained by depositing a layer of dopamine on the surface of Fe_2O_3. Firstly, 2 g Fe_2O_3 powders were distributed in tris-buffer solution (100 mL, pH = 8.5) by ultrasonication for 1 h. Then, 120, 240, and 360 mg of dopamine hydrochloride were added to the suspensions (the mass ratios of Fe_2O_3 and dopamine hydrochloride were 50:3, 50:6, and 50:9), respectively, and the suspensions were magnetically stirred in the presence of oxygen for 24 h. After that, the sediments were gathered via centrifugation then dried at 70 °C in an oven. The above synthesized Fe_2O_3@PDA precursors were successively named as Fe_2O_3@PDA-1, Fe_2O_3@PDA-2, and Fe_2O_3@PDA-3. The Fe_2O_3@PDA-4 sample was obtained by the second polymerization of dopamine on the surface of Fe_2O_3@PDA-2, the mass ratio of Fe_2O_3@PDA-2 and dopamine hydrochloride was 50:6.

2.4 Synthesis of yolk–shelled (Fe/FeO_x)@C composites

The Fe_2O_3@PDA-1, Fe_2O_3@PDA-2, and Fe_2O_3@PDA-3 precursors were reduced under an atmosphere of H_2/Ar (v/v = 5:95) at 700 °C for 3 h in a horizontal tubular furnace, then the atmosphere was switched to air as them cooled down. The products were named as (Fe/FeO_x)@C-1, (Fe/FeO_x)@C-2, and (Fe/FeO_x)@C-3, respectively. Similarly, the Fe@C composite was obtained by heating Fe_2O_3@PDA-4 composite at 700 °C for 3 h under H_2/Ar (v/v = 5:95). The Fe/FeO_x composite was obtained using Fe_2O_3 as the precursor directly in the same experiment condition. The (Fe/FeO_x)@C-600 was obtained by heating Fe_2O_3@PDA-2 at 600 °C for 4 h in H_2/Ar with a cooling process in air.

2.5 Characterizations

The morphologies and microstructures of the products were investigated by field emission scanning electron microscopy (FESEM, Zeiss Sigma) and transmission electron microscopy (TEM, FEI F20). The crystal phases of the products were investigated by X-ray diffraction (XRD) meter (Rigaku) with Cu Kα radiation. The surface information of the products was conducted by X-ray photo-electron spectroscopy (XPS, AXIS SUPRA$^+$). Raman spectra were obtained by a confocal Raman spectroscopy system (X-ploRA). The magnetic properties of the products were characterized using a vibrating sample magnetometer (VSM, Lake Shore 7404).

2.6 Electromagnetic measurements

The (Fe/FeO_x)@C/paraffin samples were made into coaxial rings with an inner diameter of 3.0 mm and an outer diameter of 7.0 mm, the mass ratio of (Fe/FeO_x)@C powders and paraffin wax was 6:4. The electromagnetic parameters of the samples in the frequency range of 2–18 GHz were obtained by an Agilent vector network analyzer (N5222A) using the coaxial-line method.

3 Results and discussion

Figure 1 displays the synthesis process of yolk–shelled (Fe/FeO_x)@C composites schematically. Briefly, the Fe_2O_3@PDA composites were prepared by coating a PDA layer on the surface of Fe_2O_3 particles via an *in-situ* polymerization in the presence of oxygen. After that, the Fe_2O_3@PDA precursors were heated at 700 °C for 3 h under a reducing atmosphere (H_2/Ar). Dopamine can polymerize on the surface of almost any material under weak base condition (pH = 8.5), which is beneficial to achieve a good uniform coating of materials and maintain the morphology after carbonization. So it is used as a carbon source in the present case. During the high-temperature reduction of Fe_2O_3@PDA composites, the Fe_2O_3 core was gradually reduced to Fe and began to shrink due to the loss of O components, resulting in the unique yolk–shell structure. Meanwhile, the PDA layer was carbonized into an amorphous carbon shell, and cracks or holes could occur in the thinner parts of the carbon shell due to the evaporation of H_2O. By introducing air in the cooling process, the surfaces of few particles that are not well encased in carbon shells were re-oxidized. As the PDA shell thickness increases, the cracking of carbon shells can be reduced and the oxidation degree will decrease. It should be pointed out that the thickness of PDA shell cannot be arbitrarily increased by a single deposition of dopamine. If the concentration of dopamine in the reaction solution is too high, the dopamine will polymerize in the solution rather than on the surface of materials. The yolk–shelled Fe@C composite was obtained by the secondary deposition of PDA and making the cooling process take place in a reductive atmosphere, which provides considerable feasibility for the study of structure–activity relationship.

The morphologies of the as-prepared Fe_2O_3 particles were observed by SEM, indicating the products are ellipsoids with an average length of 2.2 μm (Figs. S1(a) and S1(b) in the Electronic Supplementary Material (ESM)). The crystal structure of Fe_2O_3 particles was confirmed by XRD pattern (Fig. S1(c) in the ESM), in which all diffraction peaks belong to pure α-Fe_2O_3 (JCPDS No. 33–0664). As shown in Figs. 2(a)–2(c), the Fe_2O_3@PDA composites remain ellipsoidal after the polymerization. The

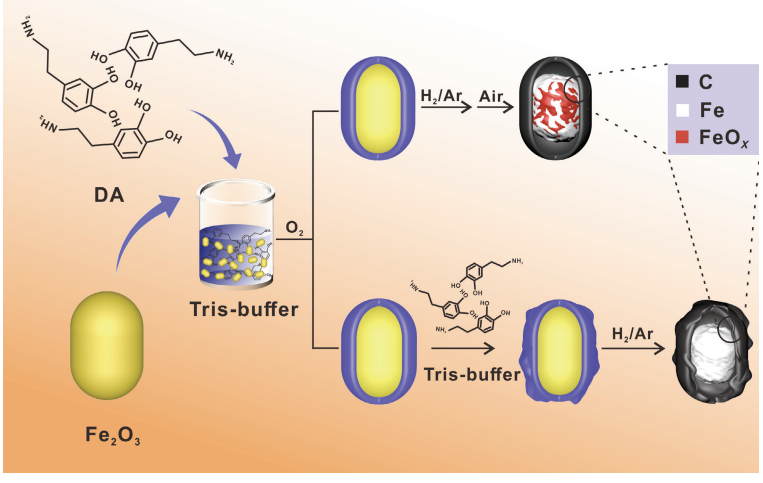

Figure 1 Schematic diagram of the synthesis process of yolk–shelled (Fe/FeO_x)@C and Fe@C composites.

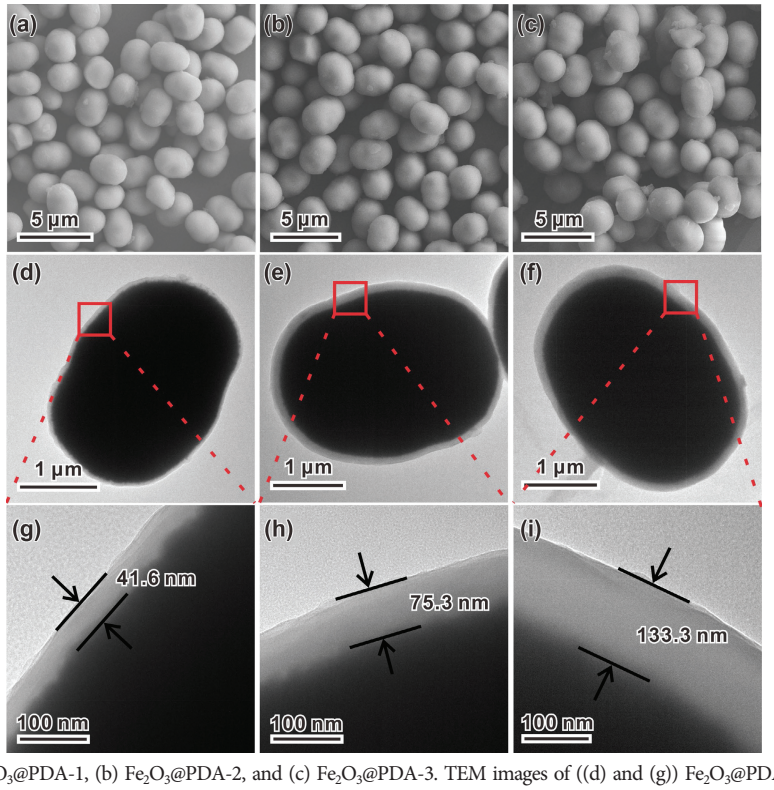

Figure 2 SEM images of (a) Fe_2O_3@PDA-1, (b) Fe_2O_3@PDA-2, and (c) Fe_2O_3@PDA-3. TEM images of ((d) and (g)) Fe_2O_3@PDA-1, ((e) and (h)) Fe_2O_3@PDA-2, and ((f) and (i)) Fe_2O_3@PDA-3.

core–shell structures of the Fe_2O_3@PDA composites can be identified by TEM images (Figs. 2(d)–2(f)). The typical PDA shell thicknesses of Fe_2O_3@PDA-1, Fe_2O_3@PDA-2, and Fe_2O_3@PDA-3 are 41.6, 75.3, and 133.3 nm, respectively (Figs. 2(g)–2(i)), indicating the PDA layer thickness can be adjusted easily by controlling the adding amount of dopamine hydrochloride to some degree. Because the PDA layer is amorphous, the XRD patterns of Fe_2O_3@PDA composites remain as α-Fe_2O_3 (Fig. S1(d) in the ESM).

Figure 3 displays the morphology and composition of the as-prepared (Fe/FeO_x)@C composites. The well-maintained ellipsoid shapes of (Fe/FeO_x)@C composites were observed in Figs. 3(a)–3(c). The XRD results show all samples have strong diffraction peaks near 44.7°, 65.0°, and 82.5°, which fit well with the body-centered cubic Fe (JCPDS No. 06–0696) (Figs. 3(d)–3(f)). In addition, weak peaks of iron oxides are also observed. For (Fe/FeO_x)@C-1 sample, three relatively weak diffraction peaks at 36.0°, 41.8°, and 60.5° are attributed to FeO (JCPDS No. 06–0615) phase. For the other two samples, the diffraction peak at 35.4° belongs to the (311) crystal plane of Fe_3O_4 (JCPDS No. 19–0629). The diffraction peak intensity ratio of iron oxide to iron can reflect the oxidation degree of iron to a certain extent. Compared to Fe and iron oxides, the XRD diffraction intensity of carbon shell for the (Fe/FeO_x)@C composites is too weak to be observed. The existence and the graphitization degree of carbon shells were revealed by Raman spectrum. Generally, there are two characteristic peaks at 800–2000 cm^{-1} in a typical Raman spectrum, the D band (~ 1350 cm^{-1}) is caused by out-of-plane vibrations due to the presence of lattice disorders or defects in materials, and the G band (~ 1580 cm^{-1}) results from the in-plane vibrations of the sp^2-bonded carbon atoms in a two-dimensional (2D) hexagonal lattice [33]. Usually, the higher I_D/I_G value represents the lower graphitization degree of carbon component. As shown in Fig. S2 in the ESM, the I_D/I_G values of (Fe/FeO_x)@C-1, (Fe/FeO_x)@C-2, and (Fe/FeO_x)@C-3 were 0.93, 0.91, and 0.94, confirming the carbon shells of the composites are mainly amorphous carbon. Elemental mappings (Fig. 3(g)) indicate the yolk–shell structure, where C distributes throughout the grain and slightly enriches at the edges, Fe is located in the smaller area of the core area of carbon distribution, and O occurs with almost the same shape of Fe.

TEM and high-resolution TEM (HRTEM) were used to characterize the structures and heterogeneous interfaces of the (Fe/FeO_x)@C composites (Fig. 4). Due to the different contrast between metal and carbon, clear gaps between the carbon shells and the magnetic cores can be observed, identifying the yolk–shell structures of the products (Figs. 4(a)–4(c)). As the PDA layer thickness increases, the carbon shell thicknesses also increase gradually for the three samples, which are 38.0, 64.8, and 121.4 nm, respectively (Figs. 4(d)–4(f)). The HRTEM image of carbon shell shows irregular stripes (Fig. 4(g)), suggesting its amorphous characteristics. The visible lattice fringes of 0.24 and 0.26 nm in Fig. 4(h) are well matched with the (111) and (310) planes of the cubic Fe_3O_4 and the orientation anisotropy of different FeO_x particles can also be observed. These results demonstrate the partial oxidation of the Fe core and the existence of Fe/FeO_x, FeO_x/air, and FeO_x/FeO_x heterogeneous interfaces. The magnetic Fe-based heterogeneous interfaces may contribute to the magnetic coupling and pinning effects, leading to better magnetic loss ability and microwave absorption performances.

The surface chemical composition and valence information of the samples were investigated by XPS spectra, and all the samples show obvious signals of C 1s, O 1s, Fe $2p_{2/3}$, and Fe $2p_{1/2}$ (Fig. 5 and Fig. S3 in the ESM). Specifically, the peaks at about 284.7, 531.6, 710.31, and 725.2 eV in Fig. 5(a) are attributed to C 1s, O 1s, Fe $2p_{2/3}$, and Fe $2p_{1/2}$, respectively. The existence of carbon-containing function groups is confirmed by the C 1s spectra. As shown in Fig. 5(b), the C 1s spectra can be fitted into three peaks, the peak at 284.7 eV is related to C–C groups, and the peaks at 286.1 and 288.8 eV correspond to C–OH or C–O–C groups and carboxyl or ester groups, respectively [34, 35]. The O 1s spectra indicates the presence of Fe_3O_4 and adsorbed oxygen-

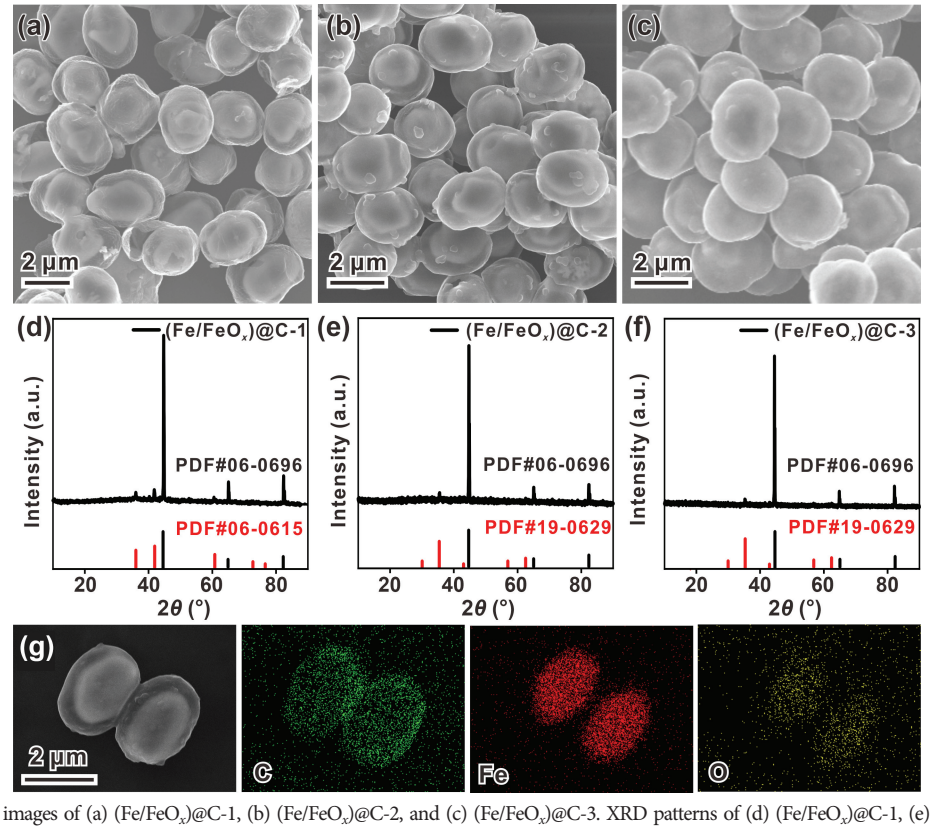

Figure 3 Typical SEM images of (a) (Fe/FeO_x)@C-1, (b) (Fe/FeO_x)@C-2, and (c) (Fe/FeO_x)@C-3. XRD patterns of (d) (Fe/FeO_x)@C-1, (e) (Fe/FeO_x)@C-2, and (f) (Fe/FeO_x)@C-3. (g) Elemental maps of the (Fe/FeO_x)@C-2 composite.

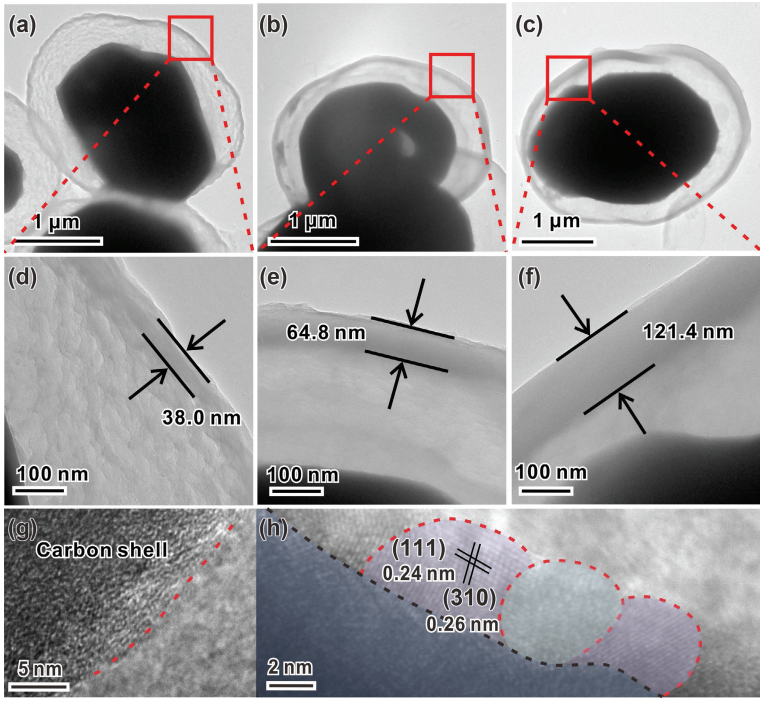

Figure 4 Typical TEM images of the as-prepared (Fe/FeO$_x$)@C composites. ((a) and (d)) (Fe/FeO$_x$)@C-1, ((b) and (e)) (Fe/FeO$_x$)@C-2, and ((c) and (f)) (Fe/FeO$_x$)@C-3. ((g) and (h)) The HRTEM images of (Fe/FeO$_x$)@C-2.

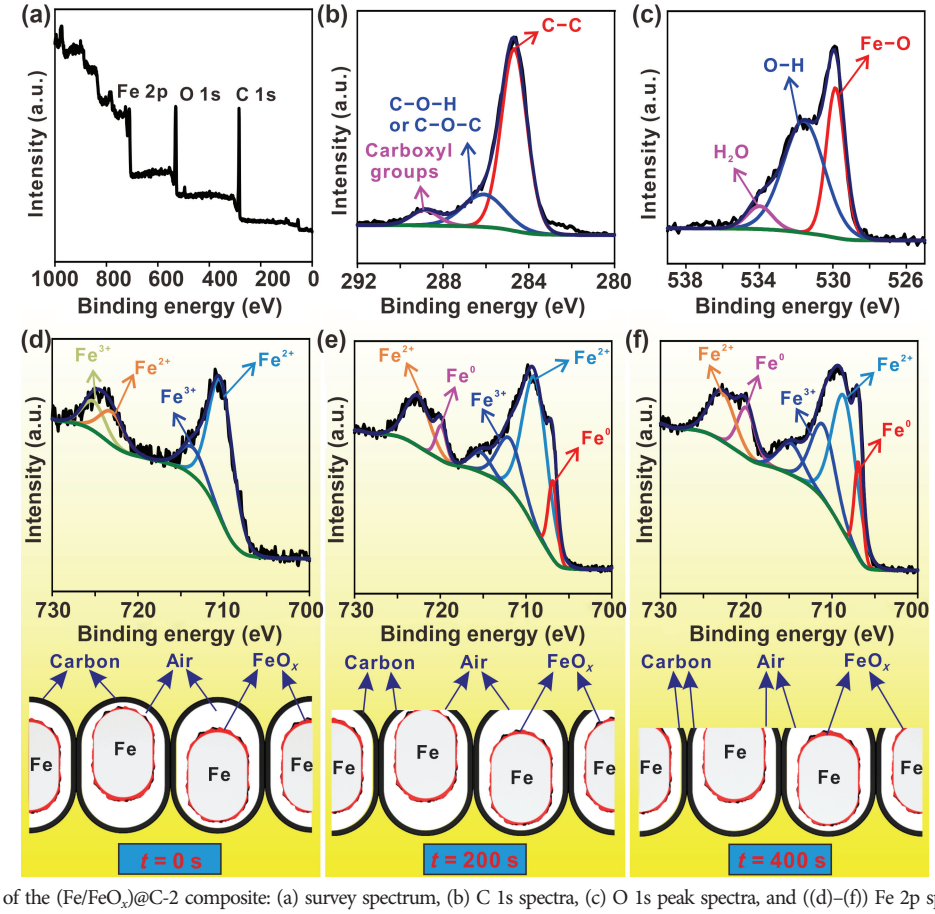

Figure 5 XPS spectra of the (Fe/FeO$_x$)@C-2 composite: (a) survey spectrum, (b) C 1s spectra, (c) O 1s peak spectra, and ((d)–(f)) Fe 2p spectra and schematics of exposed surface structures under different sputtering times.

containing groups, where the peaks (Fig. 5(c)) located at 530.0, 531.6, and 533.9 eV belong to lattice oxygen (Fe–O), adsorbed oxygen-containing groups, and H_2O, respectively [18, 34]. In order to explore the longitudinal distribution of different Fe valence states of the (Fe/FeO$_x$)@C composites, XPS depth profiles for the samples were conducted via argon ion sputtering technology. By applying appropriate sputtering intensity and time, the sample surface can be etched to different depths to get subsurface information. Taking the (Fe/FeO$_x$)@C-2 composite as an example, Figs. 5(d)–5(f) show the Fe 2p spectra and schematics of exposed surface structures under different sputtering times. When the sputtering time t = 0, the peaks located at around

710.31 and 723.03 eV are attributed to the Fe $2p_{3/2}$ and the Fe $2p_{1/2}$ spin-orbit of Fe^{2+}. Figure 5(d) shows the fitted Fe 2p spectra, in which the peaks located at around 710.31 and 723.03 eV are attributed to the Fe $2p_{3/2}$ and the Fe $2p_{1/2}$ spin-orbit of Fe^{2+} species, and the peaks centered around 713.63 and 725.15 eV are assigned to the Fe $2p_{3/2}$ configuration and the Fe $2p_{1/2}$ configuration of Fe^{3+} species (Fig. 5(d)) [35]. Although the X-ray diffraction peaks of metallic Fe are much stronger than that of Fe_3O_4, the Fe^0 signal is much inferior to those of Fe^{2+} and Fe^{3+} due to the partial surface oxidization of Fe^0 and restricted detection depth of the XPS technique [18]. When the sputtering time t = 200 s, a certain depth of carbon shell near the sample surface is destroyed, resulting in a small amount of Fe_3O_4 and Fe core exposed to the detection environment, and two obvious photoelectron peaks of Fe $2p_{3/2}$ and Fe $2p_{1/2}$ configurations of Fe^0 can be observed, which are located at 706.9 and 720.0 eV, respectively (Fig. 5(e)). As increasing the sputtering time to 400 s, a considerable part of Fe core is disclosed, and the characteristic peak intensity of Fe^0 also increases (Fig. 5(f)). The content of Fe^0 can be expressed by the peak-area ratio $[S_{Fe^0}/(S_{Fe^0}+S_{Fe^{2+}}+S_{Fe^{3+}})]$ [35]. By analyzing the Fe 2p spectra of the (Fe/FeO_x)@C-2 composite under different sputtering times, it is revealed that the peaking area ratio $[S_{Fe^0}/(S_{Fe^0}+S_{Fe^{2+}}+S_{Fe^{3+}})]$ increases from 0, 0.178, to 0.186 with the increase of sputtering time. These results indicate the oxidation degrees of the samples can be changed by adjusting the adding amount of dopamine. It also reveals that the magnetic core is composed of outer iron oxides and central iron, which is consistent with XRD and TEM results.

The magnetic hysteresis loops of the (Fe/FeO_x)@C composites were tested at room temperature, which are all S-shaped with typical ferromagnetic characteristics (Fig. S4 in the ESM). Due to the presence of amorphous carbon and iron oxides, the final products all possess lower M_s value than that of bulk Fe (217 emu/g) [36]. As a result, the coercivity and saturation magnetization values are 24.5 Oe and 167 emu/g, 23.5 Oe and 158 emu/g, and 27.6 Oe and 154 emu/g, corresponding to (Fe/FeO_x)@C-1, (Fe/FeO_x)@C-2, and (Fe/FeO_x)@C-3 (Table S1 in the ESM), respectively. The M_s values of the three samples show a downward trend, which may be caused by the increasing carbon component [22].

To investigate the MA properties of the yolk–shelled (Fe/FeO_x)@C composites, the f-dependent reflection loss (RL) values in 2–18 GHz with given d were calculated on the basis of transmission line theory using Eqs. (1) and (2) [37, 38]. Where Z_0, Z_{in}, and c represent the impedance of the free space, the input impedance of the absorber, and the speed of light, respectively

$$\mathrm{RL\,(dB)} = 20\lg\left|\frac{Z_{in}-Z_0}{Z_{in}+Z_0}\right| \quad (1)$$

$$Z_{in} = Z_0\sqrt{\frac{\mu_r}{\varepsilon_r}}\tanh\left(\mathrm{j}\frac{2\pi fd}{c}\sqrt{\mu_r\varepsilon_r}\right) \quad (2)$$

Figure 6 shows the three-dimensional (3D) and 2D RL maps of the (Fe/FeO_x)@C composites. It is obvious that all samples exhibit an advantage of multi-band microwave absorption in the thickness range of 1.0–4.5 mm. Among them, the (Fe/FeO_x)@C-2 shows the widest EAB of 7.3 GHz (10.7–18 GHz), realizing the full coverage of Ku band, and the minimum reflection loss at 13.6 GHz is −28.9 dB under 2.0 mm. At the same thickness, the other two samples also display good MA properties. The EABs of (Fe/FeO_x)@C-1 (11.0–17.7 GHz) and (Fe/FeO_x)@C-3 (10.7–17.4 GHz) are both up to 6.7 GHz, and the minimum reflection losses are −21.9 and −23.8 dB, respectively.

Aiming to find out the influence of electromagnetic parameters on the MA properties of the (Fe/FeO_x)@C composites, the relative complex permittivity ($\varepsilon_r = \varepsilon' - \mathrm{j}\varepsilon''$) and the relative complex permeability ($\mu_r = \mu' - \mathrm{j}\mu''$) of the (Fe/$FeO_x$)@C/paraffin composites were compared (Fig. 7). The ε' and μ' represent the storage capacities of electric energy and magnetic energy, and ε'' and μ'' represent the attenuation capacities of electric energy and magnetic energy, respectively [39]. The ε' values of (Fe/FeO_x)@C-1, (Fe/FeO_x)@C-2, and (Fe/FeO_x)@C-3 are in the ranges of 7.96–6.07, 8.39–6.07, and 8.03–6.21, respectively, all of them exhibit a similar trend of decrease as the frequency increases (Fig. 7(a)). This phenomenon is mainly caused by the enlargement of hysteresis of the polarization response of the dipole relative to the electric field variation as frequency increasing. The ε' values of (Fe/FeO_x)@C composites show little difference, demonstrating the carbon component has little influence on the dielectric constant within a certain thickness of the carbon layer [40]. The ε'' values of (Fe/FeO_x)@C-1, (Fe/FeO_x)@C-2, and (Fe/FeO_x)@C-3 are in the ranges of 1.47–1.76, 2.00–1.70, and 1.26–1.53, respectively (Fig. 7(b)). Based on the free electron theory [22], $\varepsilon'' \approx 1/(2\pi\rho f\varepsilon_0)$, ρ stands for resistivity, decreasing resistivity is helpful to improve the ε'' and further contributes to dielectric loss. The conductive network generated by the aggregation of adjacent Fe particles will

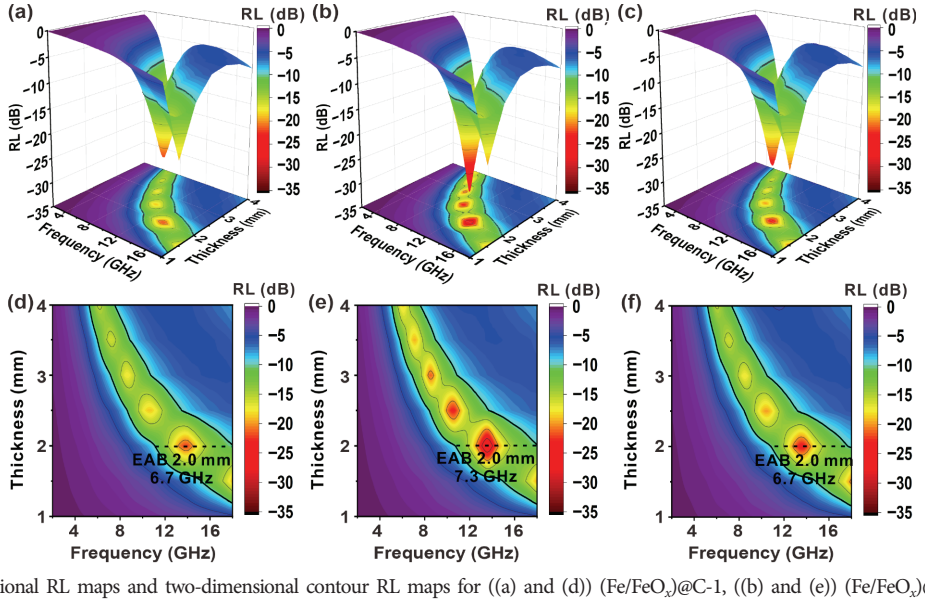

Figure 6 Three-dimensional RL maps and two-dimensional contour RL maps for ((a) and (d)) (Fe/FeO_x)@C-1, ((b) and (e)) (Fe/FeO_x)@C–2, and ((c) and (f)) (Fe/FeO_x)@C-3 composites.

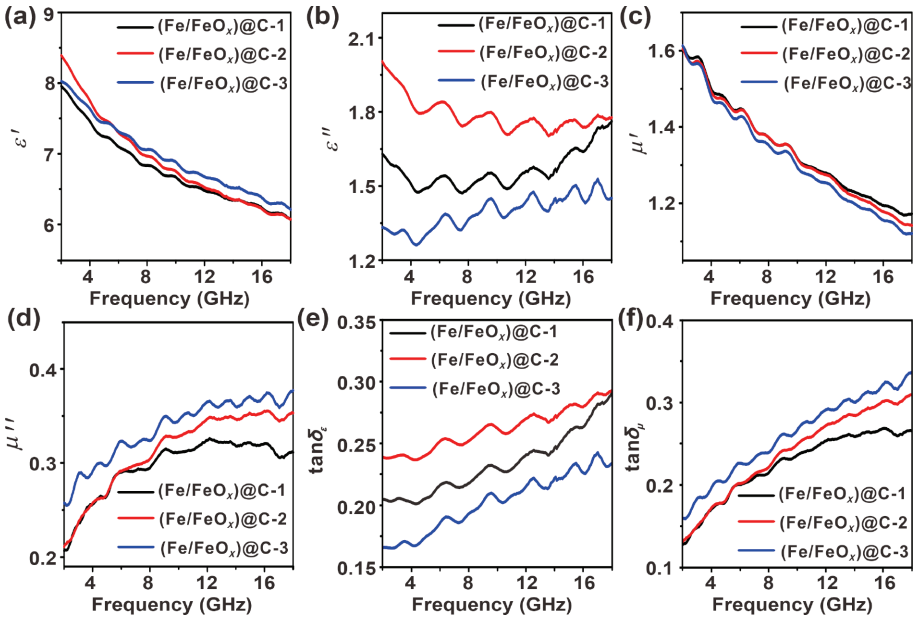

Figure 7 Frequency dependences of (a) ε', (b) ε'', (c) μ', (d) μ'', (e) $\tan\delta_\varepsilon$, and (f) $\tan\delta_\mu$ of the (Fe/FeO$_x$)@C composites.

be restrained after amorphous carbon layer coating, resulting in diminished space charge polarization [41]. Thus, the thicker carbon shell will weaken the polarization of space charge, leading to the small ε'' values of (Fe/FeO$_x$)@C-3. In addition, the fluctuations on ε'' curves are attributed to multiple polarization relaxation and conductivity in terms of Debye relaxation theory [42, 43].

According to the equation $(\mu_i - 1)f_r = 2\gamma M_s/(3\pi)$ (where μ_i is the relative initial permeability, γ is the gyromagnetic ratio, and f_r is the cut-off frequency), materials with a larger M_s usually have a higher μ' value [44]. The μ' values of (Fe/FeO$_x$)@C-1 are slightly higher than (Fe/FeO$_x$)@C-2 and (Fe/FeO$_x$)@C–3, which are in the ranges of 1.61–1.17, 1.60–1.14, and 1.61–1.12, respectively (Fig. 7(c)). This can be attributed to the higher M_s of (Fe/FeO$_x$)@C-1. All of them decrease with the increasing of frequency in the range of 2–18 GHz. In common cases, the μ'' values usually decrease as the frequency increases, especially in high frequencies [22, 41, 44–49]. On the contrary, the μ'' values of the as-prepared composites in this case all show an increasing trend in 2–18 GHz, which are in the ranges of 0.21–0.33, 0.21–0.36, and 0.25–0.38, respectively (Fig. 7(d)). The (Fe/FeO$_x$)@C-3 shows higher μ'' values than (Fe/FeO$_x$)@C-2 and (Fe/FeO$_x$)@C-1, which can be attributed to the decrease of oxidation degree. In addition, intrinsic damping, surface effects, and interactions between the particles also have an impact on the μ'' value [50]. This incremental change of μ'' may be caused by a movement of resonance frequency towards higher frequency because of the enhanced anisotropic field induced by the introduction of Fe/oxides heterointerfaces, and that will be discussed in the later part.

To better understand the MA mechanism of the (Fe/FeO$_x$)@C composites, the dielectric loss tangent ($\tan\delta_\varepsilon = \varepsilon''/\varepsilon'$) and magnetic loss tangent ($\tan\delta_\mu = \mu''/\mu'$) were calculated, which respectively determine the ability of dielectric loss and magnetic loss [48]. The $\tan\delta_\varepsilon$ values of (Fe/FeO$_x$)@C-1, (Fe/FeO$_x$)@C-2, and (Fe/FeO$_x$)@C-3 are in the ranges of 0.20–0.29, 0.24–0.29, and 0.17–0.24, and their $\tan\delta_\mu$ values are in the ranges of 0.13–0.27, 0.13–0.31, and 0.16–0.34, respectively (Figs. 7(e) and 7(f)). Usually, the dielectric loss mechanisms of absorbing materials include conductive loss and polarization loss, the latter mainly comes from dipole orientation polarization and interfacial polarization in 2–18 GHz [51, 52]. In this work, the defects in amorphous carbon shells and grain boundaries between Fe and oxides can generate dipole polarization acting as polarized centers under external electromagnetic field [22, 25]. Moreover, the charge-carriers accumulated on Fe/oxides, oxides/void, and carbon shell/air heterointerfaces will induce intensive interface polarization and dielectric relaxation on the basis of Maxwell–Wagner relaxation effect, thus improving dielectric loss ability and further enhancing the microwave absorption performance [53, 54]. The $\mu''(\mu')^{-2}f^{-1}$ values of the (Fe/FeO$_x$)@C composites cannot keep a constant as the frequency changes (Fig. S5(a) in the ESM), demonstrating natural resonance and exchange resonance are the main sources of magnetic loss resulting from magnetic coupling interaction, pinning effect, and spin wave excitation [55, 56].

Excellent impedance matching and high attenuation ability are of great significance for high-performance MAMs. The attenuation constant (α) and the impedance matching coefficient (Z) can be expressed as follows [57, 58]

$$\alpha = \frac{\pi f\sqrt{2}}{c} \times \sqrt{(\mu''\varepsilon'' - \mu'\varepsilon') + \sqrt{(\mu''\varepsilon'' - \mu'\varepsilon')^2 + (\mu'\varepsilon'' + \mu''\varepsilon')^2}} \quad (3)$$

$$Z = \left|\frac{Z_{in}}{Z_0}\right| = \left|\sqrt{\frac{\mu_r}{\varepsilon_r}}\tanh\left(j\frac{2\pi fd}{c}\sqrt{\mu_r\varepsilon_r}\right)\right| \quad (4)$$

The α values of (Fe/FeO$_x$)@C-1, (Fe/FeO$_x$)@C-2, and (Fe/FeO$_x$)@C-3 are in the ranges of 25–280, 28–299, and 25–283, respectively (Fig. S5(b) in the ESM), indicating (Fe/FeO$_x$)@C-2 owns higher attenuation ability. The Z values of (Fe/FeO$_x$)@C-1, (Fe/FeO$_x$)@C-2, and (Fe/FeO$_x$)@C-3 are in the ranges of 0.14–1.22, 0.14–1.13, and 0.14–1.18, respectively (Fig. S5(c) in the ESM). Generally, closer of impedance matching coefficient is to 1, more electromagnetic waves can enter the absorbing material. The Z values of the three samples in 2–18 GHz increase first and then decrease as the frequency increases with a turning point around 12 GHz. The maximum Z value of (Fe/FeO$_x$)@C-2 is lower than (Fe/FeO$_x$)@C-1 and (Fe/FeO$_x$)@C-3, showing better impedance matching. Therefore, a better MA property of the (Fe/FeO$_x$)@C-2 composite is reasonable.

In order to explore the effect of heterogeneous Fe/Fe$_3$O$_4$ interfaces on MA performances, the Fe@C composite was prepared using Fe$_2$O$_3$@PDA-4 (Fig. S6 in the ESM) as precursors. The morphology, structure, and phase composition of the Fe@C

composite were also investigated (Fig. 8). The SEM and TEM images (Figs. 8(a) and 8(b)) of Fe@C composite show the yolk–shell structure with a carbon shell thickness of 97.2 nm. The XRD pattern confirms that the Fe@C composite has no obvious diffraction peak of iron oxides except cubic phase Fe (Fig. 8(c)), and the presence of carbon component was proved using Raman spectroscopy (Fig. S7(a) in the ESM). The magnetic hysteresis loop of the Fe@C composite shows typical ferromagnetic characteristics with a large saturation magnetization of 177 emu/g and a low coercivity of 22.1 Oe (Fig. S7(b) in the ESM). The saturation magnetization of iron is higher than that of iron oxides, thus the iron content will affect the saturation magnetization. The higher iron content of the Fe@C sample results its larger saturation magnetization. In addition, the Fe/FeO_x interfaces in (Fe/FeO_x)@C composites play a pinning effect by hindering the rotation of the spins in the Fe core via exchange coupling effect, and a larger coercivity is needed to overcome this resistance. Thus, the coercivities of the (Fe/FeO_x)@C composites were larger than Fe@C.

The RL values and electromagnetic parameters of the (Fe/FeO_x)@C-2 composite and Fe@C composite were compared. For the Fe@C composite under 2 mm, the optimal EAB is 5.7 GHz, which is much smaller than (Fe/FeO_x)@C-2 (Figs. 8(d) and 8(e)). According to the quarter-wavelength cancellation model, the maximum RL value is achieved when the matching thickness (t_m) and the matching frequency (f_m) satisfy the equation $t_m = n\lambda/4 = nc/\left(4f_m\sqrt{|\mu||\varepsilon|}\right)$ (n = 1, 3, 5...), where c is the velocity of light [30]. Figures S8(a) and S8(b) in the ESM show the dependence of t_m and RL values on f_m for (Fe/FeO_x)@C-2 and Fe@C composites at the wavelength of $\lambda/4$. Because the $|\mu||\varepsilon|$ values of Fe@C are higher than that of (Fe/FeO_x)@C-2 in the whole tested frequency range of 2–18 GHz (Fig. S8(c) in the ESM), the minimum RL of Fe@C composite at 2 mm thickness is shifted to a lower frequency. The ε' and ε'' values of the Fe@C composite are in the ranges of 8.61–7.61 and 0.88–1.94 (Fig. 8(f)). The ε' values of the Fe@C composite are higher than (Fe/FeO_x)@C-2 in the whole testing frequency band due to its higher proportion of carbon. However, the ε'' values of (Fe/FeO_x)@C-2 are higher than Fe@C in 2–18 GHz.

The Cole–Cole curves of the (Fe/FeO_x)@C and Fe@C composites have been further investigated to analyze the contribution of ε_c'' and ε_p'' to dielectric loss. For all samples, iron is the main chemical component, resulting in low overall resistivities and contributing to establish a good conductive network, thus the values of ε_c'' are significantly greater than that of ε_p'' (Figs. S9(a) and S9(b) in the ESM). The average ε_c'' and ε_p'' values of (Fe/FeO_x)@C-1, (Fe/FeO_x)@C-2, and (Fe/FeO_x)@C-3 all are higher than Fe@C (Figs. S9(c) and S9(d)), demonstrating the finite oxidation strategy can effectively improve the dielectric loss of Fe@C composite by improving both conductive loss and polarization loss. By introducing a small amount of surface iron oxides via the finite oxidation process, the differences in Fermi energy and dielectric constant of iron and iron oxides will generate Schottky barrier to form space-charge regions and electric fields, which greatly promotes the hopping of positive and negative charges across the Fe/FeO_x heterointerfaces, thus strengthening conduction loss (Fig. S9(c) in the ESM) [59]. Meanwhile, a large number of lattice defects in the Fe/FeO_x heterointerfaces will induce the accumulation or rearrangement of spatial charges and provide abundant active sites for dipole polarization. In addition, the Fe/FeO_x and FeO_x/C heterointerfaces also generate polarizations and capacitor-like structures, and further enhance interface polarization loss. Thus, the polarization losses of the (Fe/FeO_x)@C composites are significantly improved (Fig. S9(d) in the ESM). These results demonstrate this finite oxidation strategy can effectively improve the dielectric loss of Fe@C composite by improving both conductive loss and polarization loss (Fig. 8(g)).

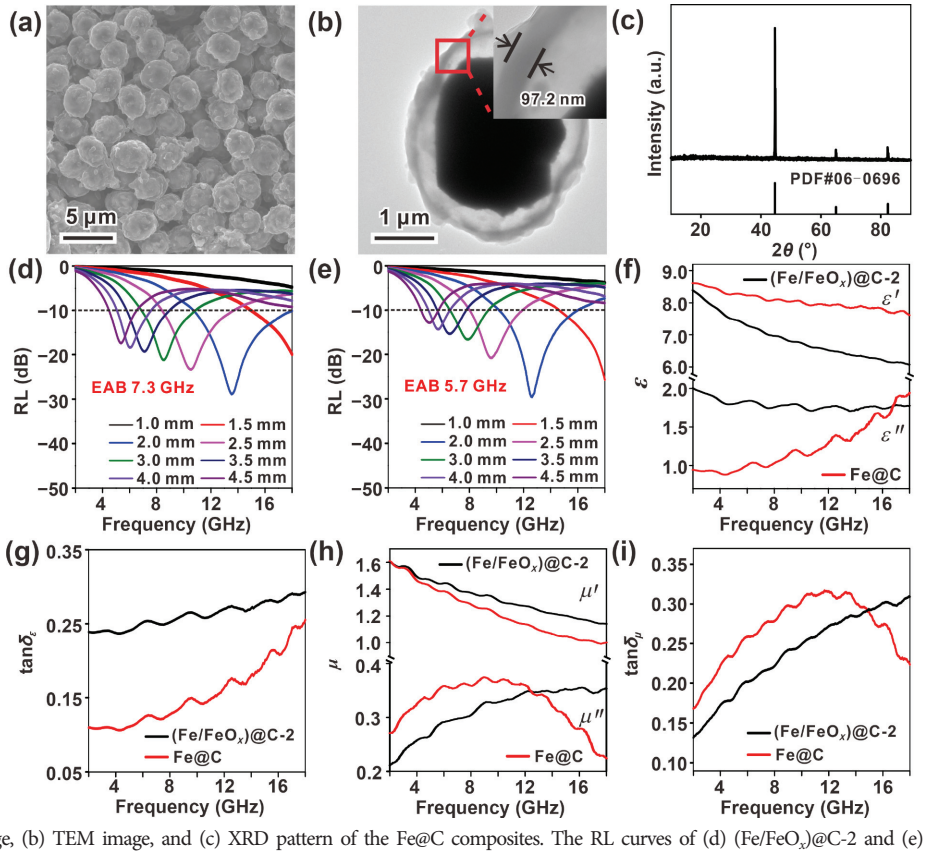

Figure 8 (a) SEM image, (b) TEM image, and (c) XRD pattern of the Fe@C composites. The RL curves of (d) (Fe/FeO_x)@C-2 and (e) Fe@C composites. The frequency dependence of (f) ε, (g) $\tan\delta_\varepsilon$, (h) μ, and (i) $\tan\delta_\mu$ of Fe@C composites, for comparison, the corresponding values of (Fe/FeO_x)@C-2 are also shown in these figures.

The μ' and μ'' values of the Fe@C composite are in the ranges of 1.61–0.99 and 0.22–0.37 (Fig. 8(h)). The μ' values of Fe@C are smaller than (Fe/FeO_x)@C-2 (Fig. 8(h)), which may be caused by the pinning effect of lattice defects in Fe/Fe_3O_4 heterogeneous interfaces and magnetic coupling effect between Fe and Fe_3O_4, leading to decreased domain wall displacement and improved stray magnetic field energy [60]. The μ'' curve of Fe@C shows some fluctuations, which may be caused by natural resonance and exchange resonance resulting from magnetic coupling interaction, pinning effect, and spin wave excitation. According to the following equation [22, 47, 61]: $3\pi f_r = \gamma|H_c|$, where γ is the spin-magnetic ratio, the natural resonance frequency f_r will shift to higher frequency region as the H_c increases. In this work, the μ'' value of (Fe/FeO_x)@C-2 has no downtrend with the increasing frequency in the high frequency range, as well as (Fe/FeO_x)@C-1 and (Fe/FeO_x)@C-3, which can be regarded as a movement of resonance frequency towards higher frequency due to their larger coercivity than Fe@C, resulting in higher μ'' values and magnetic loss tangent values at high frequencies (Fig. 8(i)). In addition, the (Fe/FeO_x)@C-2 composite has higher α values and better impedance matching than Fe@C (Fig. S10 in the ESM). These results demonstrate that the introduction of heterogeneous Fe/Fe_3O_4 interface can adjust the ε_r and μ_r of the composites to meet a good balance by increasing polarization relaxation and promoting the shift of resonance frequency to higher frequencies.

To further explore the influences of chemical component and Fe/FeO_x heterointerfaces on the improvement of μ'', the Fe/FeO_x and (Fe/FeO_x)@C-600 composites were prepared by controlling the experimental condition. As shown in Figs. S11(a) and S11(b) in the ESM, the Fe/FeO_x particles fuse with each other due to the lack of carbon sequestration and the (Fe/FeO_x)@C-600 composite remains a complete yolk–shell structure. The XRD patterns of Fe/FeO_x and (Fe/FeO_x)@C-600 both show obvious diffraction peaks of Fe_3O_4 other than Fe, indicating the presence of Fe/FeO_x heterointerfaces and the higher oxidation degree of Fe/FeO_x (Fig. S11(c) in the ESM). The electromagnetic parameters and RL values of Fe/FeO_x and (Fe/FeO_x)@C-600 composites were also investigated (Figs. S11(d)–S11(h) in the ESM). For Fe/FeO_x, both of the ε' and ε'' values are smaller than (Fe/FeO_x)@C-2, which may be caused by the removal of carbon components. Due to the fusion of tens of micro-sized Fe/FeO_x particles, a giant cross-linked conductive network was formed, thus inducing strong eddy current and skin effect. Under the alternating magnetic field, the current will concentrate on the surface of Fe/FeO_x, resulting in the partial invalidation of internal magnetic field and the μ' and μ'' values of Fe/FeO_x decline rapidly as the frequency increases. As a result, the Fe/FeO_x composite shows poor MA performances. Compared to (Fe/FeO_x)@C-2, the ε' and ε'' values of (Fe/FeO_x)@C-600 both decrease significantly, but the μ' and μ'' values show small differences. Especially, the μ'' value of (Fe/FeO_x)@C-600 still keeps a high value in 10–18 GHz without decline, demonstrating the introduction of a small amount of iron oxides can really improve the imaginary part of the permeability at high frequencies. However, the EAB of (Fe/FeO_x)@C-600 is smaller than that of (Fe/FeO_x)@C-2, which may attribute to the weak dielectric loss and poor impedance matching caused by the decreased permittivity. Thus, a proper reduction temperature is important for achieving good impedance matching and MA properties.

The MA mechanisms of the yolk–shelled (Fe/FeO_x)@C composites are summarized as shown in Fig. 9. Firstly, the yolk–shell structure greatly improves the impedance matching by introducing large air space in the composite, which makes more microwaves enter the absorbing materials easier. And it also extends the propagation path and time of microwaves in absorbing materials by enhancing multiple reflections and scattering, and ultimately promotes the attenuation of incident microwaves [62]. Secondly, the space charges, lattice defects, surface functional groups of amorphous carbon shells, and heterogeneous interfaces of Fe/FeO_x, inside air/carbon shell, FeO_x/inside air, and carbon shell/air & paraffin can be seen as "genes" and play a great "gene effect" in dielectric loss [63, 64]. On the one hand, the difference in the Fermi level (E_F) between FeO_x and Fe will lead to built-in electric fields and space-charge regions at the interfaces, which contribute to the electro transport and the spatial micro-current fields, thus increasing conduction loss [20]. On the other hand, the rich defects in amorphous carbon shells and magnetic heterointerfaces can act as polarized centers to promote dipole polarization. Meanwhile, the abundant heterointerfaces will induce the accumulation of charge carriers, which contributes to increase polarization relaxation and provide a strong dielectric loss capability. The most importantly, the introduction of FeO_x is beneficial for the shift of resonance frequency to higher frequency due to its high surface anisotropy and the Fe/FeO_x interfaces also play an importance role in pinning effect and magnetic coupling, thus leading to better magnetic loss ability and excellent MA performance.

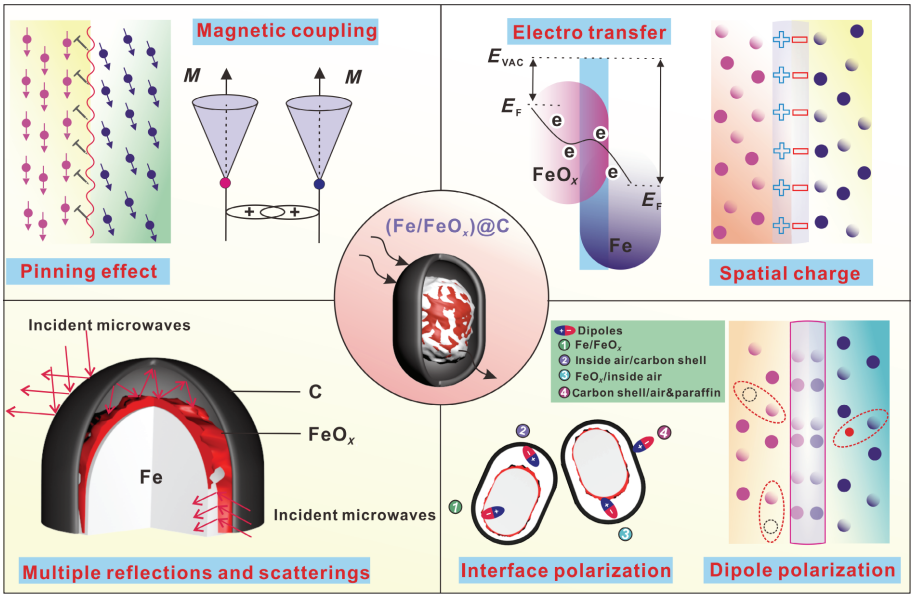

Figure 9 Schematic description of possible microwave absorption mechanisms of the (Fe/FeO_x)@C composites.

4 Conclusions

In summary, in order to explore the effect of partial surface oxidation of iron particles on their MA properties, yolk–shelled (Fe/FeO_x)@C composites have been successfully prepared via a finite oxidation strategy. It is concluded that the performance enhancements are attributed to the accelerated electro transport and the build of spatial micro-current fields by the difference in the E_F between FeO_x and Fe, the increased dipole polarization and interface polarization by the rich defects in the composite, and the improved permeability by the movement of resonance frequency towards the higher frequency range. Meanwhile, the yolk–shell structure can effectively improve impedance matching and enhance microwave absorption performances via increasing multiple reflection and scattering behaviors of incident microwaves. The (Fe/FeO_x)@C-2 composites with partial surface oxidized iron cores show the best performance, the minimum reflection loss is −28.9 dB at 13.6 GHz, and the EAB can reach 7.3 GHz (10.7–18 GHz) at 2.0 mm. This work provides a new insight into the development of ferromagnetic/carbon materials with broad-band effective absorption at a small thickness.

Acknowledgements

This work was supported by the National Natural Science Foundation of China (Nos. 21771151 and 21931009) and the Natural Science Foundation of Fujian Province of China (No. 2022J01042).

Electronic Supplementary Material: Supplementary material (the morphology, size, and the phase composition of Fe_2O_3 particles; the XRD pattern of Fe_2O_3@PDA composites; Raman spectra, XPS spectra, magnetic hysteresis loops, α, Z, ε_c'', ε_p'', and $\mu''(\mu')^{-2}f^{-1}$ of the (Fe/FeO_x)@C composites; the SEM image, XRD pattern, and TEM images of Fe_2O_3@PDA-4; t_m and $|\varepsilon||\mu|$ of (Fe/FeO_x)@C-2 and Fe@C; SEM images, XRD patterns, RL, ε', ε'', μ', and μ'' of Fe/FeO_x and (Fe/FeO_x)@C-600) is available in the online version of this article at https://doi.org/10.1007/s12274-023-5511-7.

References

[1] Cao, M. S.; Wang, X. X.; Zhang, M.; Cao, W, Q.; Fang, X. Y.; Yuan, J. Variable-temperature electron transport and dipole polarization turning flexible multifunctional microsensor beyond electrical and optical energy. *Adv. Mater.* **2020**, *32*, 1907156.

[2] Balci, O.; Polat, E. O.; Kakenov, N.; Kocabas, C. Graphene-enabled electrically switchable radar-absorbing surfaces. *Nat. Commun.* **2015**, *6*, 6628.

[3] Cao, M. S.; Song, W. L.; Hou, Z. L.; Wen, B.; Yuan, J. The effects of temperature and frequency on the dielectric properties, electromagnetic interference shielding and microwave-absorption of short carbon fiber/silica composites. *Carbon* **2010**, *48*, 788–796.

[4] Song, Q.; Ye, F.; Kong, L.; Shen, Q. L.; Han, L. Y.; Feng, L.; Yu, G. J.; Pan, Y. A.; Li, H. J. Graphene and MXene nanomaterials: Toward high-performance electromagnetic wave absorption in gigahertz band range. *Adv. Funct. Mater.* **2020**, *30*, 2000475.

[5] Cao, M. S.; Wang, X. X.; Zhang, M.; Shu, J. C.; Cao, W. Q.; Yang, H. J.; Fang, X. Y.; Yuan, J. Electromagnetic response and energy conversion for functions and devices in low-dimensional materials. *Adv. Funct. Mater.* **2019**, *29*, 1807398.

[6] Xiao, J. X.; Qi, X. S.; Gong, X.; Peng, Q.; Chen, Y. L.; Xie, R.; Zhong, W. Defect and interface engineering in core@shell structure hollow carbon@MoS_2 nanocomposites for boosted microwave absorption performance. *Nano Res.* **2022**, *15*, 7778–7787.

[7] Li, H.; Bao, S. S.; Li, Y. M.; Huang, Y. Q.; Chen, J. Y.; Zhao, H.; Jiang, Z. Y.; Kuang, Q.; Xie, Z. X. Optimizing the electromagnetic wave absorption performances of designed Co_3Fe_7@C yolk–shell structures. *ACS Appl. Mater. Interfaces* **2018**, *10*, 28839–28849.

[8] Gai, L. X.; Zhao, H. H.; Wang, F. Y.; Wang, P.; Liu, Y. L.; Han, X, J.; Du, Y. C. Advances in core–shell engineering of carbon-based composites for electromagnetic wave absorption. *Nano Res.* **2022**, *15*, 9410–9439.

[9] Li, X. A.; Du, D. X.; Wang, C. S.; Wang, H. Y.; Xu, Z. P. *In situ* synthesis of hierarchical rose-like porous Fe@C with enhanced electromagnetic wave absorption. *J. Mater. Chem. C* **2018**, *6*, 558–567.

[10] Zhou, X. D.; Han, H.; Wang, Y. C.; Zhang, C.; Lv, H. L.; Lou, Z. C. Silicon-coated fibrous network of carbon nanotube/iron towards stable and wideband electromagnetic wave absorption. *J. Mater. Sci. Technol.* **2022**, *121*, 199–206.

[11] Qing, Y. C.; Zhou, W. C.; Jia, S.; Luo, F.; Zhu, D. M. Microwave electromagnetic property of SiO_2-coated carbonyl iron particles with higher oxidation resistance. *Phys. B Condens. Matter* **2011**, *406*, 777–780.

[12] Liu, G.; Wang, L. Y.; Yang, Z. H.; Wu, R. B. Synthesis of iron-based hexagonal microflakes for strong microwave attenuation. *J. Alloys Compd.* **2017**, *718*, 46–52.

[13] Javid, M.; Zhou, Y. L.; Zhou, T. H.; Wang, D. X.; Zhou, L.; Shah, A.; Duan, Y. P.; Dong, X. L.; Zhang, Z. D. *In-situ* fabrication of Fe@ZrO_2 nanochains for the heat-resistant electromagnetic wave absorber. *Mater. Lett.* **2019**, *242*, 199–202.

[14] Duan, W. J.; Li, X. D.; Wang, Y.; Qiang, R.; Tian, C. H.; Wang, N.; Han, X. J.; Du, Y. C. Surface functionalization of carbonyl iron with aluminum phosphate coating toward enhanced anti-oxidative ability and microwave absorption properties. *Appl. Surf. Sci.* **2018**, *427*, 594–602.

[15] Wang, Y. C.; Wang, W. L.; Sun, J.; Sun, C. G.; Feng, Y. K.; Li, Z. Microwave-based preparation and characterization of Fe-cored carbon nanocapsules with novel stability and super electromagnetic wave absorption performance. *Carbon* **2018**, *135*, 1–11.

[16] Manna, P. K.; Yusuf, S. M. Two interface effects: Exchange bias and magnetic proximity. *Phys. Rep.* **2014**, *535*, 61–99.

[17] Nogués, J.; Sort, J.; Langlais, V.; Skumryev, V.; Suriñach, S.; Muñoz, J. S.; Baró, M. D. Exchange bias in nanostructures. *Phys. Rep.* **2005**, *422*, 65–117.

[18] Li, X. A.; Qu, X. Y.; Xu, Z.; Dong, W. Q.; Wang, F. Y.; Guo, W. C.; Wang, H. Y.; Du, Y. C. Fabrication of three-dimensional flower-like heterogeneous Fe_3O_4/Fe particles with tunable chemical composition and microwave absorption performance. *ACS Appl. Mater. Interfaces* **2019**, *11*, 19267–19276.

[19] Chen, F.; Luo, H.; Cheng, Y. Z.; Liu, J. L.; Wang, X.; Gong, R. Z. Fe/Fe_3O_4@N-doped carbon hexagonal plates decorated with Ag nanoparticles for microwave absorption. *ACS Appl. Nano Mater.* **2019**, *2*, 7266–7278.

[20] Liang, L. L.; Gu, W. H.; Wu, Y.; Zhang, B. S.; Wang, G. H.; Yang, Y.; Ji, G. B. Heterointerface engineering in electromagnetic absorbers: New insights and opportunities. *Adv. Mater.* **2022**, *34*, 2106195.

[21] Liu, Q. C.; Zi, Z. F.; Zhang, M.; Pang, A. B.; Dai, J. M.; Sun, Y. P. Enhanced microwave absorption properties of carbonyl iron/Fe_3O_4 composites synthesized by a simple hydrothermal method. *J. Alloys Compd.* **2013**, *561*, 65–70.

[22] Wang, X. L.; Geng, Q. Y.; Shi, G. M.; Xu, G.; Yu, J.; Guan, Y. Y.; Zhang, Y. J.; Li, D. One-pot solvothermal synthesis of Fe/Fe_3O_4 composites with broadband microwave absorption. *J. Alloys Compd.* **2019**, *803*, 818–825.

[23] Xu, C. Y.; Liu, P. B.; Wu, Z. C.; Zhang, H. B.; Zhang, R. X.; Zhang, C.; Wang, L.; Wang, L. Y.; Yang, B. T.; Yang, Z. Q. et al. Customizing heterointerfaces in multilevel hollow architecture constructed by magnetic spindle arrays using the polymerizing-etching strategy for boosting microwave absorption. *Adv. Sci.* **2022**, *9*, 2200804.

[24] Sun, D. P.; Zou, Q.; Wang, Y. P.; Wang, Y. J.; Jiang, W.; Li, F. S. Controllable synthesis of porous Fe_3O_4@ZnO sphere decorated graphene for extraordinary electromagnetic wave absorption. *Nanoscale* **2014**, *6*, 6557–6562.

[25] Liu, Q. H.; Cao, Q.; Bi, H.; Liang, C. Y.; Yuan, K. P.; She, W.;

Yang, Y. J.; Che, R. C. CoNi@SiO_2@TiO_2 and CoNi@Air@TiO_2 microspheres with strong wideband microwave absorption. *Adv. Mater.* **2016**, *28*, 486–490.
[26] Chen, N.; Dong, Z.; Wang, X. Y.; Guan, Z. J.; Jiang, J. T.; Wang, K. J. Construction of $FeNi_3$ and core–shell structured $FeNi_3$@C microspheres toward broadband electromagnetic wave absorbing. *Appl. Surf. Sci.* **2022**, *603*, 154337.
[27] Mao, R. J.; Bao, S. S.; Li, Q. S.; Yuan, Y. S.; Liang, Z. H.; Zhang, M. X.; Jiang, Z. Y.; Xie, Z. X. Rational design of two-dimensional flaky Fe/void/C composites for enhanced microwave absorption properties. *Dalton Trans.* **2022**, *51*, 8705–8713.
[28] Bao, S. S.; Song, Z. J.; Mao, R. J.; Li, Y.; Zhang, S. H.; Jiang, Z. Y.; Li, X. A.; Xie, Z. X. Synthesis of hollow rod-like hierarchical structures assembled by CoFe/C nanosheets for enhanced microwave absorption. *J. Mater. Chem. C* **2021**, *9*, 13860–13868.
[29] Dong, W. Q.; Li, X. A.; Tang, H. M.; Shi, K.; Wang, C. S.; Guo, W. C.; Tian, K. S.; Wang, H. Y. Electromagnetic attenuation distribution in a three-dimensional amorphous carbon matrix with highly dispersed Fe/Fe_3C@graphite-C nanoparticles. *Mater. Des.* **2022**, *216*, 110528.
[30] Liu, Y.; Li, Y. N.; Jiang, K. D.; Tong, G. X.; Lv, T. X.; Wu, W. H. Controllable synthesis of elliptical Fe_3O_4@C and Fe_3O_4/Fe@C nanorings for plasmon resonance-enhanced microwave absorption. *J. Mater. Chem. C* **2016**, *4*, 7316–7323.
[31] Zhou, T. D.; Zhou, P. H.; Liang, D. F.; Deng, L. J. Structure and electromagnetic characteristics of flaky FeSiAl powders made by melt-quenching. *J. Alloys Compd.* **2009**, *484*, 545–549.
[32] Liu, X.; Qiao, L.; Li, F. S. Microwave properties in relation to magnetic anisotropy of the $Nd(Fe_{1-x}Co_x)_{10}V_2$ system. *J. Phys. D: Appl. Phys.* **2010**, *43*, 165004.
[33] Gao, S. T.; Zhang, Y. C.; Xing, H. L.; Li, H. X. Controlled reduction synthesis of yolk–shell magnetic@void@C for electromagnetic wave absorption. *Chem. Eng. J.* **2020**, *387*, 124149.
[34] Liu, L.; He, Z. D.; Zhao, Y. T.; Sun, J. C.; Tong, G. X. Modulation of the composition and surface morphology of expanded graphite/Fe/Fe_3O_4 composites for plasmon resonance-enhanced microwave absorption. *J. Alloys Compd.* **2018**, *765*, 1218–1227.
[35] Liu, Y.; Fu, Y. W.; Liu, L.; Li, W.; Guan, J. G.; Tong, G. X. Low-cost carbothermal reduction preparation of monodisperse Fe_3O_4/C core–shell nanosheets for improved microwave absorption. *ACS Appl. Mater. Interfaces* **2018**, *10*, 16511–16520.
[36] Park, J. H.; Lee, S.; Chul Ro, J.; Suh, S. J. Yolk–shell Fe-Fe_3O_4@C nanoparticles with excellent reflection loss and wide bandwidth as electromagnetic wave absorbers in the high-frequency band. *Appl. Surf. Sci.* **2022**, *573*, 151469.
[37] Guan, Z. J.; Jiang, J. T.; Yan, S. J.; Sun, Y. M.; Zhen, L. Sandwich-like cobalt/reduced graphene oxide/cobalt composite structure presenting synergetic electromagnetic loss effect. *J. Colloid Interface Sci.* **2020**, *561*, 687–695.
[38] Zhang, R. X.; Wang, L.; Xu, C. Y.; Liang, C. Y.; Liu, X. H.; Zhang, X. F.; Che, R. C. Vortex tuning magnetization configurations in porous Fe_3O_4, nanotube with wide microwave absorption frequency. *Nano Res.* **2022**, *15*, 6743–6750.
[39] Du, Y. C.; Liu, W. W.; Qiang, R.; Wang, Y.; Han, X. J.; Ma, J.; Xu, P. Shell thickness-dependent microwave absorption of core–shell Fe_3O_4@C composites. *ACS Appl. Mater. Interfaces* **2014**, *6*, 12997–13006.
[40] Wang, H.; Guo, H. H.; Dai, Y. Y.; Geng, D. Y.; Han, Z.; Li, D.; Yang, T.; Ma, S.; Liu, W.; Zhang, Z. D. Optimal electromagnetic-wave absorption by enhanced dipole polarization in Ni/C nanocapsules. *Appl. Phys. Lett.* **2012**, *101*, 083116.
[41] Zhang, Z. Y.; Liu, X. X.; Wang, X. J.; Wu, Y. P.; Liu, Y. Electromagnetic and microwave absorption properties of Fe-$Sr_{0.8}La_{0.2}Fe_{11.8}Co_{0.2}O_{19}$ shell–core composites. *J. Magn. Magn. Mater.* **2012**, *324*, 2177–2182.
[42] Liu, P. B.; Gao, S.; Wang, Y.; Zhou, F. T.; Huang, Y.; Luo, J. H. Metal-organic polymer coordination materials derived Co/N-Doped porous carbon composites for frequency-selective microwave absorption. *Compos. B Eng.* **2020**, *202*, 108406.
[43] Zhu, X. J.; Dong, Y. Y.; Pan, F.; Xiang, Z.; Liu, Z. C.; Deng, B. W.; Zhang, X.; Shi, Z.; Lu, W. Covalent organic framework-derived hollow core–shell Fe/Fe_3O_4@porous carbon composites with corrosion resistance for lightweight and efficient microwave absorption. *Compos. Commun.* **2021**, *25*, 100731.
[44] Wei, H. Y.; Zhang, Z. P.; Hussain, G.; Zhou, L. S.; Li, Q.; Ostrikov, K. Techniques to enhance magnetic permeability in microwave absorbing materials. *Appl. Mater. Today* **2020**, *19*, 100596.
[45] Li, X. A.; Dong, W. Q.; Zhang, C.; Guo, W. C.; Wang, C. S.; Li, Y. M.; Wang, H. Y. Leaf-like Fe/C composite assembled by iron veins interpenetrated into amorphous carbon lamina for high-performance microwave absorption. *Compos. Part A: Appl. Sci. Manuf.* **2021**, *140*, 106202.
[46] Li, X. P.; Deng, Z. M.; Li, Y.; Zhang, H. B.; Zhao, S.; Zhang, Y.; Wu, X. Y.; Yu, Z. Z. Controllable synthesis of hollow microspheres with Fe@carbon dual-shells for broad bandwidth microwave absorption. *Carbon* **2019**, *147*, 172–181.
[47] Zhang, X. F.; Dong, X. L.; Huang, H.; Liu, Y. Y.; Wang, W. N.; Zhu, X. G.; Lv, B.; Lei, J. P.; Lee, C. G. Microwave absorption properties of the carbon-coated nickel nanocapsules. *Appl. Phys. Lett.* **2006**, *89*, 053115.
[48] Zhang, H. Y.; Cao, F.; Xu, H.; Tian, W.; Pan, Y.; Mahmood, N.; Jian, X. Plasma-enhanced interfacial engineering of FeSiAl@PUA@SiO_2 hybrid for efficient microwave absorption and anti-corrosion. *Nano Res.* **2023**, *16*, 645–653.
[49] Wu, Y. H.; Wang, G. D.; Yuan, X. X.; Fang, G.; Li, P.; Ji, G. B. Heterointerface engineering in hierarchical assembly of the Co/$Co(OH)_2$@carbon nanosheets composites for wideband microwave absorption. *Nano Res.* **2023**, *16*, 2611–2691.
[50] Han, Z.; Li, D.; Wang, H.; Liu, X. G.; Li, J.; Geng, D. Y.; Zhang, Z. D. Broadband electromagnetic-wave absorption by FeCo/C nanocapsules. *Appl. Phys. Lett.* **2009**, *95*, 023114.
[51] Bao, S. S.; Tang, W.; Song, Z. J.; Jiang, Q. R.; Jiang, Z. Y.; Xie, Z. X. Synthesis of sandwich-like $Co_{15}Fe_{85}$@C/RGO multicomponent composites with tunable electromagnetic parameters and microwave absorption performance. *Nanoscale* **2020**, *12*, 18790–18799.
[52] Ma, W. J.; He, P.; Wang, T. Y.; Xu, J.; Liu, X. Y.; Zhuang, Q. X.; Cui, Z. K.; Lin, S. L. Microwave absorption of carbonization temperature-dependent uniform yolk–shell H-Fe_3O_4@C microspheres. *Chem. Eng. J.* **2021**, *420*, 129875.
[53] Li, J.; Wang, L.; Zhang, D.; Qu, Y.; Wang, G. M.; Tian, G.; Liu, A. H.; Yue, H. J.; Feng, S. H. Reduced graphene oxide modified mesoporous FeNi alloy/carbon microspheres for enhanced broadband electromagnetic wave absorbers. *Mater. Chem. Front.* **2017**, *1*, 1786–1794.
[54] Wang, J. Y.; Wang, Z. H.; Liu, R. G.; Li, Y. X.; Zhao, X. N.; Zhang, X. F. Heterogeneous interfacial polarization in Fe@ZnO nanocomposites induces high-frequency microwave absorption. *Mater. Lett.* **2017**, *209*, 276–279.
[55] Feng, A. L.; Jia, Z. R.; Zhao, Y.; Lv, H. L. Development of Fe/Fe_3O_4@C composite with excellent electromagnetic absorption performance. *J. Alloys Compd.* **2018**, *745*, 547–554.
[56] Meng, F. B.; Wei, W.; Chen, X. N.; Xu, X. L.; Jiang, M.; Jun, L.; Wang, Y.; Zhou, Z. W. Design of porous C@Fe_3O_4 hybrid nanotubes with excellent microwave absorption. *Phys. Chem. Chem. Phys.* **2016**, *18*, 2510–2516.
[57] Li, C.; Qi, X. S.; Gong, X.; Peng, Q.; Chen, Y. L.; Xie, R.; Zhong, W. Magnetic–dielectric synergy and interfacial engineering to design yolk–shell structured CoNi@void@C and CoNi@void@C@MoS_2 nanocomposites with tunable and strong wideband microwave absorption. *Nano Res.* **2022**, *15*, 6761–6771.
[58] Li, N.; Huang, G. W.; Li, Y. Q.; Xiao, H. M.; Feng, Q. P.; Hu, N.; Fu, S. Y. Enhanced microwave absorption performance of coated carbon nanotubes by optimizing the Fe_3O_4 nanocoating structure. *ACS Appl. Mater. Interfaces* **2017**, *9*, 2973–2983.
[59] Lu, M. M.; Cao, W. Q.; Shi, H. L.; Fang, X. Y.; Yang, J.; Hou, Z. L.; Jin, H. B.; Wang, W. Z.; Yuan, J.; Cao, M. S. Multi-wall carbon nanotubes decorated with ZnO nanocrystals: Mild solution-process synthesis and highly efficient microwave absorption properties at elevated temperature. *J. Mater. Chem. A* **2014**, *2*, 10540–10547.
[60] You, W. B.; Che, R. C. Excellent NiO-Ni nanoplate microwave absorber via pinning effect of antiferromagnetic–ferromagnetic

interface. *ACS Appl. Mater. Interfaces* **2018**, *10*, 15104–15111.
[61] Qiao, M. T.; Lei, X. F.; Ma, Y.; Tian, L. D.; He, X. W.; Su, K. H.; Zhang, Q. Y. Application of yolk–shell Fe_3O_4@N-doped carbon nanochains as highly effective microwave-absorption material. *Nano Res.* **2018**, *11*, 1500–1519.
[62] Liu, X. F.; Hao, C. C.; He, L. H.; Yang, C.; Chen, Y. B.; Jiang, C. B.; Yu, R. H. Yolk–shell structured Co-C/void/Co_9S_8 composites with a tunable cavity for ultrabroadband and efficient low-frequency microwave absorption. *Nano Res.* **2018**, *11*, 4169–4182.
[63] Yao, L. H.; Cao, W. Q.; Zhao, J. G.; Zheng, Q.; Wang, Y. C.; Jiang, S.; Pan, Q. L.; Song, J.; Zhu, Y. Q.; Cao, M. S. Regulating bifunctional flower-like $NiFe_2O_4$/graphene for green EMI shielding and lithium ion storage. *J. Mater. Sci. Technol.* **2022**, *127*, 48–60.
[64] Wang, X. X.; Zhang, M.; Shu, J. C.; Wen, B.; Cao, W. Q.; Cao, M. S. Thermally-tailoring dielectric "genes" in graphene-based heterostructure to manipulate electromagnetic response. *Carbon* **2021**, *184*, 136–145.